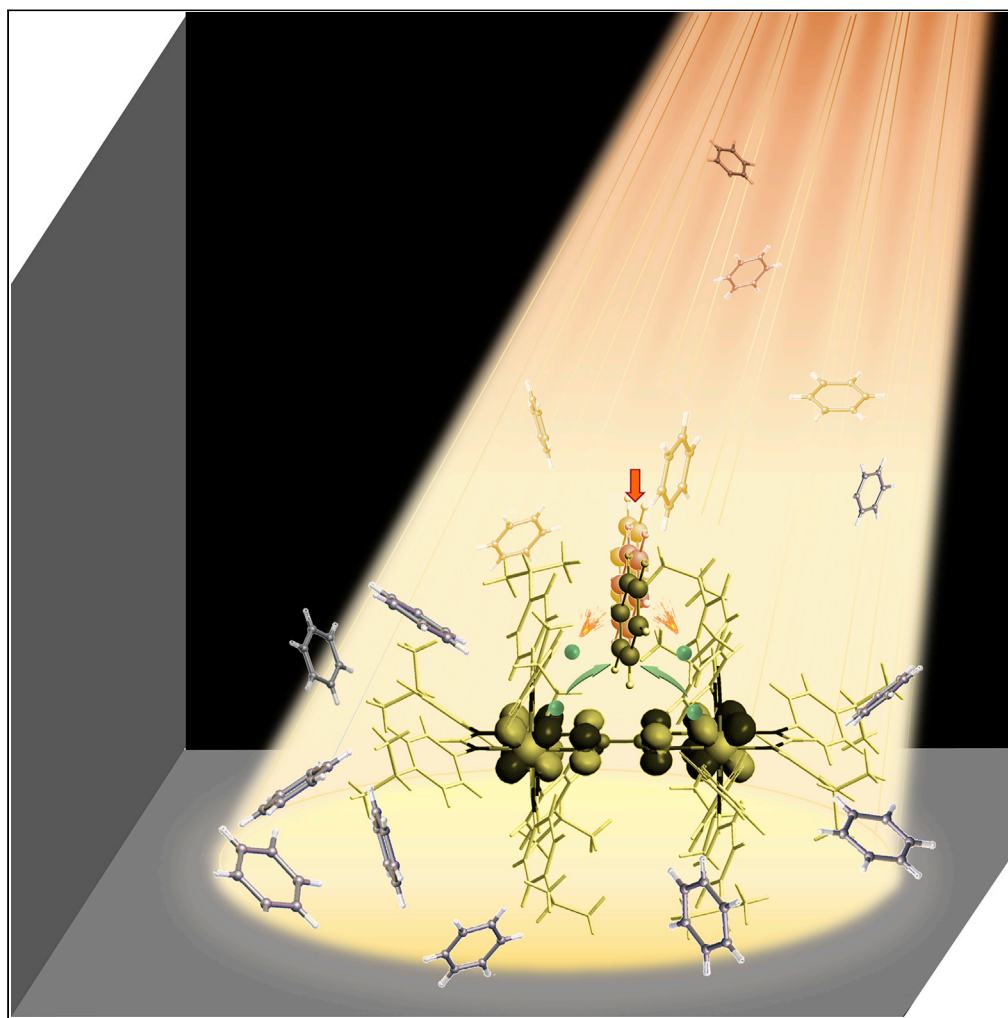**Article**

A single solvating benzene molecule decouples the mixed-valence complex through intermolecular orbital interactions

Suman Mallick, Yuli Zhou, Xiaoli Chen, ..., Tao Cheng, Guang Yuan Zhu, Chun Y. Liu

tcyliu@jnu.edu.cn (C.Y.L.)
tmengm@jnu.edu.cn (M.M.)

Highlights

Decoupling mixed-valence complexes by an encapsulated benzene molecule

Demonstrating intermolecular orbital interactions in the van der Waals distances

Illustrating interplay between intermolecular electronic and nuclear degrees of freedom

Article

A single solvating benzene molecule decouples the mixed-valence complex through intermolecular orbital interactions

Suman Mallick,[1,2] Yuli Zhou,[1,2] Xiaoli Chen,[1,2] Ying Ning Tan,[1] Miao Meng,[1,*] Lijiu Cao,[1] Yi Qin,[1] Zi Cong He,[1] Tao Cheng,[1] Guang Yuan Zhu,[1] and Chun Y. Liu[1,3,*]

SUMMARY

Characterization of covalency of intermolecular interactions in the van der Waals distance limit remains challenging because the interactions between molecules are weak, dynamic, and not measurable. Herein, we approach this issue in a series of supramolecular mixed-valence (MV) donor(D)-bridge(B)-acceptor(A) systems consisting of two bridged Mo_2 units with a C_6H_6 molecule encapsulated, as characterized by the X-ray crystal structures. Comparative analysis of the inter-valence charge transfer spectra in benzene and dichloromethane substantiates the strong electronic decoupling effect of the solvating C_6H_6 molecule that breaks down the dielectric solvation theory. *Ab initio* and DFT calculations unravel that the intermolecular orbital overlaps between the complex bridge and the C_6H_6 molecule alter the electronic states of the D-B-A molecule through intermolecular nuclear dynamics. This work exemplifies that site-specific intermolecular interaction can be exploited to control the chemical property of supramolecular systems and to elucidate the functionalities of side-chains in biological systems.

INTRODUCTION

Interatomic and intermolecular interactions account for the formation of uncountable, all kinds of matter on the earth from the limited number of chemical elements, fragments, and molecules, and are responsible for DNA and the evolutionary development of any organism. These two types of basic forces are distinguished from each other in terms of the spatial range that affects the strength and physical origin. Covalent bonds are formed by orbital overlaps or electron sharing between the adjacent atoms or atoms nearby within the molecule, which determines the chemical properties of the molecules. In general awareness, non-covalent bonding is dominated by permanent and/or inductive dipole interactions, i.e., van der Waals forces, which are electrostatic in nature and affect the physical properties of compounds. However, the nature of the non-covalent bonds has been questioned throughout the history of valence theory (Kaplan, 2006; Kellett et al., 2020). Many efforts have been devoted to explore the covalency of intermolecular interactions (Chalasinski and Szczesniak, 1994; Jeziorski et al., 1994) in systems such as hydrogen-bonded clusters (Isaacs et al., 1999; Grabowski, 2011) and small molecular adducts (Grabowski, 2018; Tsuzuki et al., 2000) or dimers (Chalasinski and Szczesniak, 1994; Jeziorski et al., 1994; Kaplan, 2006). The recognition of the covalent character of hydrogen bonds has led to the recent revision of IUPAC definition of H-bonding (Arunan et al., 2011). Orbital interactions between molecules in the van der Waals distances and the underlying effects are unclear for two reasons: (i) the Pauli repulsion exchange energy that offsets the attractive non-covalent contribution (Chalasinski and Szczesniak, 1994; Jeziorski et al., 1994); (ii) lack of technical means for experimental investigation. On the other hand, the energetical, structural, and constitutional dynamics of intermolecular interactions endow the multiple-component system assembled through non-covalent bonding with programmable, tunable ,and reversible chemical and/or physical properties. Therefore, detailed understanding on intermolecular interactions benefits the development of functional complex matters and smart materials with supramolecular arrays (Lehn, 2002, 2007).

Solvent effects on intramolecular electron transfer (ET) have been a long-standing research topic (Biasin et al., 2021; Chen and Meyer, 1998; Marcus and Sutin, 1985) in understanding intermolecular interactions that affect the elementary chemical reactions. In Marcus theory, the increase of nuclear vibrational energy for ET in a condensed medium is termed as the solvent or outer reorganization energy (λ_o) that becomes

[1]Department of Chemistry, Jinan University, 601 Huang-Pu Avenue West, Guangzhou 510632, China

[2]These authors contributed equally

[3]Lead contact

*Correspondence:
tcyliu@jnu.edu.cn (C.Y.L.),
tmengm@jnu.edu.cn (M.M.)

part of the total reorganization energy λ, i.e., $\lambda = \lambda_i + \lambda_o$, where λ_i is the intramolecular vibrational or inner reorganization energy (Chen and Meyer, 1998; Marcus and Sutin, 1985). Whereas λ_i is constant in different solvents, according to the dielectric continuum theory (Marcus and Sutin, 1985), λ_o increases with increasing solvent polarity (Chen and Meyer, 1998; Heckmann and Lambert, 2012). Research endeavors on solvent effects deal with basically the solute–solvent electrostatic interactions and the averaged behaviors of randomly moving solvent molecules (Lear et al., 2007). It is known that local solute–solvent interactions affect the chemical potential of the solute molecule and, thus, the intramolecular ET dynamics (Chen and Meyer, 1998). Paddon–Row and Zimmt reported that an aromatic molecule filled in the cleft of a U-shaped (Napper et al., 2002) or C-clamp (Kumar et al., 1996; Nadeau et al., 2003) donor(D)-bridge(B)-acceptor(A) molecule accelerates the photoinduced electron transfer. In Kubiak's group, it was observed that the non-covalent host–guest interaction between the calix[6]arene and the auxiliary ligands (4-phenyl pyridine) on the Ru_3-Ru_3 mixed valence (MV) ion caused the electronic coupling to decrease (Lear and Kubiak, 2007). Recently, we demonstrated that an Mo_2-Mo_2 MV complex is substantially decoupled by quadruple–quadruple interactions between an aromatic solvent molecule and the thienylene bridge of the D-B-A molecule (Mallick et al., 2019). Moreover, ultrafast reorientation of a local solvent molecule coupled to intramolecular ET was observed lately (Biasin et al., 2021). A recent theoretical study reveals that solvation of the sodium dimer in THF alters the solute molecular identity (Widmer and Schwartz, 2018). However, overall, the nature of intermolecular interactions is not explicitly elucidated. The study of molecular dynamics/quantum mechanics has pointed out that orbitals of solvent molecules play the role in mediating the electronic coupling (EC) and controlling the ET pathways (Troisi et al., 2004), which however, has not been verified experimentally. In nature, aromatic side–chain interactions are found to be critical to some biological systems and biochemical processes (Meyer et al., 2003; Tatko and Waters, 2002; Thomas et al., 2002). With the scarce reports, our knowledge on the site-specific intermolecular interactions occurring at the van der Waals distance limits is insufficient (Biasin et al., 2021; Politzer et al., 2015), particularly in complex systems that are geometrically and electronically well defined.

Herein, we approach these concerned issues in a supramolecular MV D-B-A system that includes a C_6H_6 molecule in the cleft of the complex molecular skeleton in benzene. In this system, the encapsulated C_6H_6 molecule decouples the intramolecular electronic interaction through intermolecular interaction, as expressed by the variation in the characteristics of the intervalence charge transfer (IVCT) absorption. This allows us to circumvent the problem that intermolecular interaction is unmeasurable by analyzing the change of chemical property of the system, a way Hoffmann suggested for the study of through-space orbital interactions within a molecule (Hoffmann, 1971). *Ab initio* and DFT calculations and optical analysis show that in the supramolecular nuclear ground state, host–guest orbital interactions attenuate the intramolecular electronic coupling (EC) by interfering with the superexchange pathway, whereas in the nuclear nonequilibrium states, an increase of the ET nonadiabaticity leads to the simultaneous breakdown of the Born–Oppenheimer approximation and the Condon approximation, gating the intramolecular ET. Our results show that in the van der Waals distance limit, optimal intermolecular orbital overlaps can be achieved by best complements between the interreacting molecules in the symmetry, energy, and direction of molecular orbitals (MOs), in analogy to interatomic orbital interactions. This study provides new insights into intermolecular nuclei–electron interactions.

RESULTS

Molecular synthesis and structural characterization

Following the procedures developed in our laboratory (Tan et al., 2017; Xiao et al., 2013; Zhu et al., 2021), a series of three dimeric complexes of Mo_2 were synthesized by assembling two dimolybdenum building blocks $[Mo_2(DIppF)_3]^+$ (DIppF = N, N'-di(*p*-isopropylphenyl)formamidinate) with an oxalate-type bridging ligand $[EE'C-CEE']^{2-}$ (E, E' = O or S). With stepwise substitution of sulfur atoms for the oxygen chelating atoms, the bridged Mo_2 dimers, denoted as **1**, **2**, and **3**, respectively, share a common molecular skeleton and have similar structural geometries. In previous work, the DAniF (N, N'-di(*p*-anisyl)formamidinate) MV analogues of this series were studied for their strong and exceptionally strong EC interactions (Tan et al., 2017). In this work, the DippF auxiliary ligands were chosen to increase the solubility of the complex in the non-polar solvents benzene and hexafluorobenzene.

Diffusion of ethanol into a benzene solution of the complex produced single crystals suitable for X-ray diffraction for each of the Mo_2 dimers, which led to the determination of the molecular structures, as shown in Figure 1. For all molecules of this series, the molecular architecture features topologically two clefts built
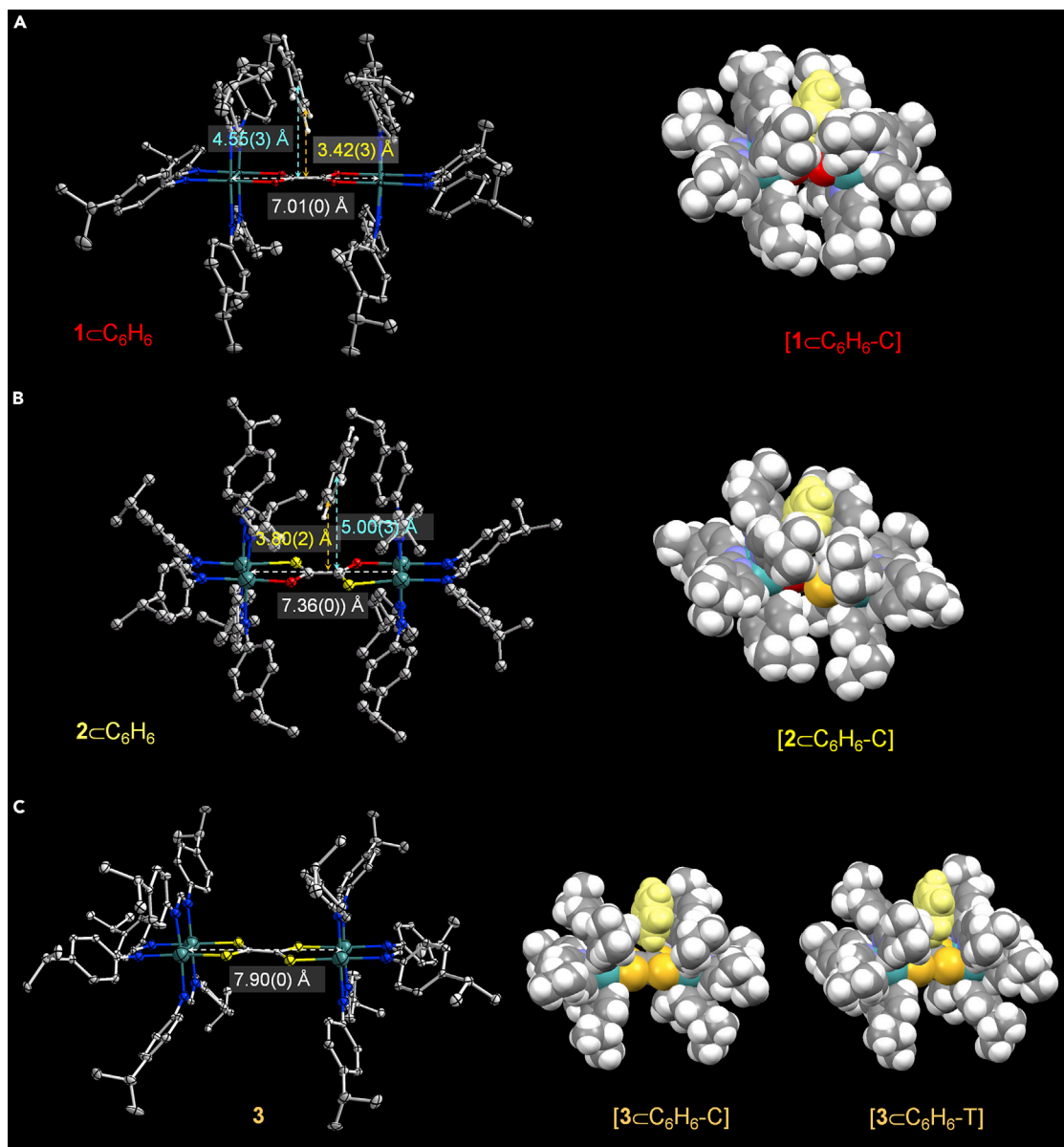
Figure 1. Molecular structures of the Mo$_2$ dimers with a captured benzene molecule in the cleft and the corresponding DFT optimized C$_6$H$_6$-included supramolecular space-filling models

The structures are drawn with displacement ellipsoids at the 30% probability levels. The hydrogen atoms are omitted except for those on the solvating C$_6$H$_6$ molecules. In the supramolecular space-filling models, the C$_6$H$_6$ molecule is included in the cleft with either crossing (C) or T-shaped (T) geometric modes.

(A) Crystal structure of **1**⊂C$_6$H$_6$ and the singly C$_6$H$_6$ solvated space-filling model [**1**⊂C$_6$H$_6$-C].

(B) Crystal structure of **2**⊂C$_6$H$_6$ and space-filling model [**2**⊂C$_6$H$_6$-C].

(C) Crystal structure of **3** and the space-filling models [**3**⊂C$_6$H$_6$-C] and [**3**⊂C$_6$H$_6$-T].

by the vertically arranged formamidinate ligands on the two Mo$_2$ units that are deepened by substituting DIppF for DAniF (Tan et al., 2017). For **1** and **2**, there is one benzene molecule embedded in the clefts, forming a supramolecular structure, designated as **1**⊂C$_6$H$_6$ and **2**⊂C$_6$H$_6$, but, interestingly, in the crystal structure, the clefts of **3** are unoccupied (Figure 1). The central C(1)−C(2) bond distance of the bridging ligand decreases as the chelating O atoms are successively replaced by S atoms, that is, 1.526(3) Å (**1**), 1.494(8) Å (**2**), and 1.483(5) Å (**3**), showing an increased π electron density on the bridge for complexes with more S atoms. The Mo$_2$•••Mo$_2$ separation, which determines the width of the clefts, varies in the opposite direction, increasing from 7.009(0) Å (**1**) to 7.358(0) Å (**2**) to 7.902(0) Å (**3**) (Figure 1 and
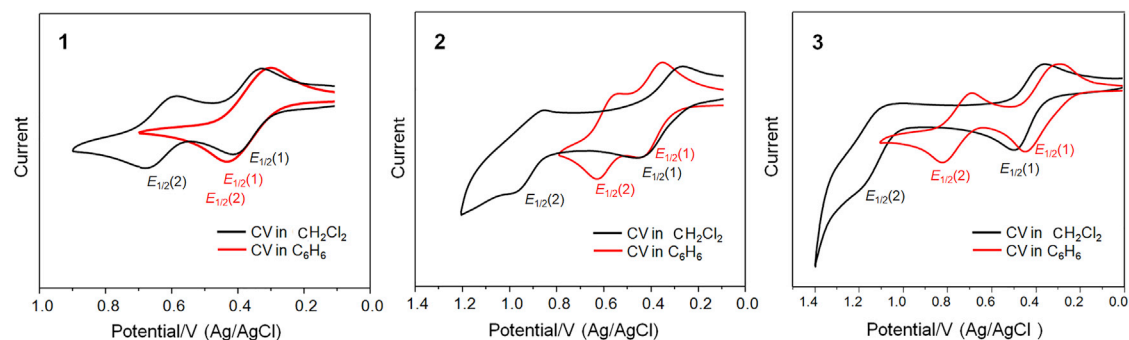
Figure 2. Electrochemical cyclic voltammograms (CVs) for the complexes 1, 2 and 3 in DCM (black) and benzene (red)
The redox potential separations ($\Delta E_{1/2}$) were measured from the $E_{1/2}$ (1) and $E_{1/2}$ (2) values, except for **1** in benzene. The $\Delta E_{1/2}$ value for **1** in benzene was estimated from the working curve using the Richardson–Taube method (Richardson and Taube, 1981) (Figure S10 and Table S5). The $E_{1/2}$ value of Fc^+/Fc^0 standard is 0.49 V under the experimental condition.

Table S4). Notably, this distance for $1 \subset C_6H_6$ is appreciably longer than that for the structure of **1** without capturing a C_6H_6 molecule in the cleft (Table S4). Presumably, the inclusion of a C_6H_6 molecule in $1 \subset C_6H_6$ has caused slight structural distortion of the cleft. The guest C_6H_6 molecule in the cleft is situated on the bridge with the two neighboring H atoms crossing the C-C bond, which is denoted as the crossing mode (C) (Figure 1). The mass center of C_6H_6 is separated from the plane defined by the two Mo_2 units by 4.55(3) Å for $1 \subset C_6H_6$ and by 5.00(3) Å for $2 \subset C_6H_6$, and the shortest intermolecular non-hydrogen contacts are 3.42 (2) and 3.80(2) Å, respectively, as shown in Figures 1A and 1B. Therefore, the C_6H_6 molecule in 1 is confined tightly by contacting both walls and the bottom of the cleft in the lowest limit of van der Waals distances, whereas in $2 \subset C_6H_6$, the guest molecule in the cleft is slightly loose (Figures 1A and 1B). For 1 and **2**, but not for **3**, the O•••H contacts between the complex bridge and the benzene molecule, 2.69(6) Å for $1 \subset C_6H_6$ and 3.34(1) Å for $2 \subset C_6H_6$, may improve the intermolecular binding affinity through molecular recognition (Christopher, 2004).

Solvent-dependent electrochemistry, spectroscopy, and electronic coupling of the Mo_2 D-B-A complexes

Compounds 1, **2**, and **3** in DCM show two well-resolved reversible redox waves in the cyclic voltammograms (CVs) (Figure 2), attributed to the successive one-electron oxidations occurring on one of the Mo_2 centers and then on the other (Xiao et al., 2013), that is, $Mo_2(IV)-Mo_2(IV) \rightarrow Mo_2(V)-Mo_2(IV)$ and $Mo_2(V)-Mo_2(IV) \rightarrow Mo_2(V)-Mo_2(V)$. The redox potential separations ($\Delta E_{1/2}$) increase from 260 (**1**) to 560 (**2**) to 700 mV (**3**), larger than those for the DAniF analogues owing to the stronger electron donation of DIppF (Tan et al., 2017). In benzene, however, the $\Delta E_{1/2}$ values (Figure 2 and Table 1) tremendously decrease to 82, 190, and 380 mV, respectively, suggesting a significant electronic decoupling effect. These results, resembling the observations for the thienylene bridged analogues in aromatic solvents (Mallick et al., 2019), do not conform to the dielectric continuum model that predicts enhanced EC in less polar solvents. Assuming that the Mo_2•••Mo_2 separations in DCM and benzene remain unchanged, the large decreases of $\Delta E_{1/2}$ should be attributed to substantial lowering of the resonant contribution to the overall EC (Crutchley, 1994).

The neutral complexes were converted into the corresponding MV complexes (1^+, 2^+, and 3^+) by chemical oxidation with one equivalent of ferrocenium hexafluorophosphate (Mallick et al., 2019; Tan et al., 2017). These cationic complexes were characterized by electron paramagnetic resonance (EPR) spectra *in situ*. For the MV complex series, generally termed as $[Mo_2-Mo_2]^+$, the EPR spectra show a pronounced isotropic signal with $g \approx 1.95$ (Figure S11), smaller than that of an organic free radical ($g \approx 2.0023$), indicating that the odd electron resides in the δ orbital of the Mo_2 centers (Mallick et al., 2019; Tan et al., 2017). Therefore, for the MV series, intramolecular electronic coupling occurs between the two Mo_2 units, which is mediated by the bridging ligand, as evidenced by the varied $\Delta E_{1/2}$ values (Xiao et al., 2013).

The visible to short-wave IR spectra for the cationic MV complexes 1^+, 2^+, and 3^+ were measured in DCM, C_6H_6, and C_6F_6, as shown in Figures 3A–3C. The δ→δ* transitions (Cotton and Nocera, 2000) occur in the range of 400–500 nm (25,000–20,000 cm^{-1}) as usual (Figures 3A–3C) (Tan et al., 2017; Xiao et al., 2013).

Table 1. Spectroscopic data of the IVCT bands and the EC parameters for the mixed-valence Mo_2 dimers in different solvents

Complex	$\Delta E_{1/2}$ (mV)	E_{IT} (cm^{-1})	ε_{IT} (M^{-1}cm^{-1})	$\Delta \nu_{1/2}$ (exp) (cm^{-1})	Cut-off[a] area (%)	ΔE_{H-H-1} (cm^{-1})	ΔE_{IT}[b] (cm^{-1})	H_{ab}[c] (cm^{-1})	MV Class
1^+(DCM)	260	3,766	8,283	1,531	28.1	3,145	/	1,883	Class II–III
$[1^+ \subset C_6H_6$-C]	82	4,953	2,209[d]	2,129	16.9	2,581	+1187	1,059	Class II
2^+(DCM)	560	4,086	15,869	1,135	22.6	4,194	/	2,043	Class III
$[2^+ \subset C_6H_6$-C]	190	4,782	1,440	1,392	13.2	3,952	+696	2,391	Class II–III
2^+(C$_6$F$_6$)	/	4,351	12,809	1,277	19.6	4,275	+265	2,175	Class III
3^+(DCM)	700	4,914	11,818	1,079	20.4	4,920	/	2,477	Class III
$[3^+ \subset C_6H_6$-T]	380	5,142	1,500	1,114	21.9	4,758	+188	2,571	Class III
3^+(C$_6$F$_6$)	/	5,095	11,933	1,012	13.0	5,000	+141	2,547	Class III

[a]For each of the systems, the cut-off area is measured from the difference between the observed IVCT bandwidth at half-height ($\Delta \nu_{1/2}$(exp)) and the Gaussian-shape simulated half-height bandwidth ($\Delta \nu_{1/2}$(simu)).

[b]ΔE_{IT} refers to the change of E_{IT} in benzene relative to that in DCM (Figure S16–S20 and Table S7).

[c]For $[1^+ \subset C_6H_6$-C] (Class II), H_{ab} is calculated from the Mulliken–Hush expression (Hush, 1967; Table S7), $H_{ab} = 2.06 \times 10^{-2} \frac{(\Delta \nu_{1/2} \varepsilon_{IT} E_{IT})^{1/2}}{r_{ab}}$. Here, the effective charge transfer distance r_{ab} is 4.20 Å, determined from the centroid distance between the two Mo_2O_2C chelating rings (see Table S7). For those in Classes II–III and Class III, $H_{ab} = E_{IT}/2$ (Brunschwig et al., 2002).

[d]This value of ε_{IT} is read from the spectra (Figure 3A) based on the initial concentration of 1^+. The effective ε_{IT} for $[1^+ \subset C_6H_6$-C] is twice as large as the spectral data, considering that the effective concentration is lowered by half, owing to electronic decoupling in benzene (see Table S7).

Metal (δ) to bridging ligand (π^*) charge transfer (MLCT) and bridging ligand (π) to metal (δ) (LMCT) bands, occurring on the donor ($[Mo_2]^0$) and acceptor ($[Mo_2]^+$) sites, respectively, may be observed simultaneously for valence-trapped (Class II) complexes (Crutchley, 1994; Liu et al., 2013; Zhu et al., 2021) in line with the McConnel superexchange mechanism (McConnell, 1961). For 1^+ in DCM, two LMCT bands are observed at 16,330 and 14,740 cm^{-1}; in benzene, these two bands are blue-shifted by about 2,500 cm^{-1}, mixing with the $\delta \rightarrow \delta^*$ and MLCT bands in the high-energy region (Figure 3A and Table S6). For **2** and 2^+, similar electronic spectra are seen in benzene, which are significantly different from the spectra in DCM (Figures 3A and S12B). This indicates implicitly that in benzene, there exists the same solvation mode for the neutral and cationic complexes. Compared with **2**, the MV complex (2^+) exhibits a low-energy shoulder at 12,650 cm^{-1}, which can be assigned to the LMCT band (Figure 3B). Note that this band is not present in the spectra in DCM (Figure 3B) owing to the strong EC (Class III) (Tan et al., 2017), therefore confirming the decoupling effect of benzene. For 3^+, there is no LMCT band detected in both DCM and benzene, showing a Class III character in both solvents.

A striking spectral feature for the MV complexes in DCM is the intense near-IR IVCT absorbances in accordance with the Hush model (Brunschwig et al., 2002; D'Alessandro and Keene, 2006; Hush, 1967). The spectral characteristics are essentially the same as those for the DAniF analogues, from which the complexes can be assigned to Classes II–III (1^+) and Class III (2^+ and 3^+) (Brunschwig et al., 2002; Tan et al., 2017), in terms of the Robin–Day's classification (Robin and Day, 1967). For all the three MV complexes in benzene, the IVCT energies (E_{IT}) are commonly higher, but the band intensities much lower than in DCM (Figure 3, Table 1 and Figures S13–S18). In previous works (Tan et al., 2017; Wu et al., 2017; Xiao et al., 2013; Zhu et al., 2021), we have shown that for an MV series with similar molecular constitutions and structures, the IVCT band energy decreases as the EC increases. However, for the Class III species near the II–III borderline, which has the lowest intervalence transition energy, both increasing and reducing the extent of EC would cause a blue-shift of the IVCT band (Tan et al., 2017). Therefore, the observed IVCT band shifts toward high energy, together with a great decrease of the IVCT absorption, indicating the strong decoupling effect of benzene (Mallick et al., 2019), in agreement with the electrochemical results. For 1^+, the IVCT band maximum moves from 3,766 to 4,953 cm^{-1} as the solvent changes from DCM to benzene, showing the largest IVCT blue-shift, i.e., $\Delta E_{IT} = 1,187$ cm^{-1} (Table 1). The coupling energy H_{ab} is calculated to be 1,059 cm^{-1} from the Mulliken–Hush expression (Table 1 and Table S7) (Hush, 1967), giving $2H_{ab} < \lambda$ (= E_{IT}), which characterizes the MV system in the Class II regime (Brunschwig et al., 2002; D'Alessandro and Keene, 2006; Heckmann and Lambert, 2012). In addition, the increase of E_{IT} (1187 cm^{-1}), with an equal increase of the reorganization energy (λ) (Crutchley, 1994), implies an upsurge of the ET nonadiabaticity. However, it is interesting to note that 1^+ shows the largest blue-shift of the IVCT, which accounts for the
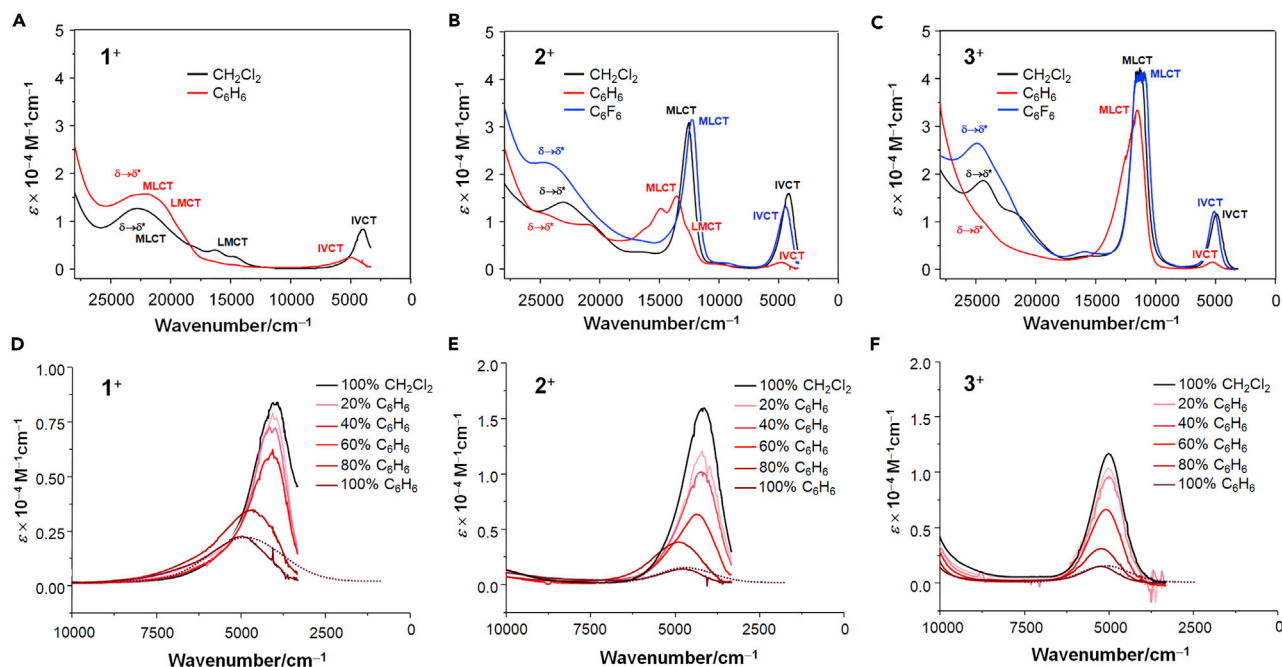
Figure 3. Visible to short-wave IR spectra of the mixed-valence complexes in DCM (black), benzene (red) and hexafluorobenzene (blue)

(A) The spectra of 1^+. For 1^+, the spectra in hexafluorobenzene were not recorded owing to the low solubility of the complex.

(B) The spectra of 2^+.

(C) The spectra of 3^+.

(D–F) Variations of the IVCT spectra in the DCM-C_6H_6 mixed solvents for 1^+, 2^+, and 3^+, respectively. For each of the complexes, the spectrum in pure benzene is fitted by a Gaussian-shaped band profile (dotted line) to show the cut-off area.

strongest decoupling effect, but exhibits the smallest reduction of molar absorptivity. In DCM, complex 1^+ has the molar extinction coefficient (ε_{IT}) smaller than those of 2^+ and 3^+ because of the relatively weak coupling, in agreement with the electrochemical results. In benzene, however, the ε_{IT} value for 1^+ is substantially larger than the data for the two analogues (Table 1), which is unparallel to the variation of IVCT transition energy. We will give detailed discussion and interpretation, through theoretic analysis, on these results that appear to be in contrast (*vide infra*). Notably, the decoupling effect of benzene observed for the MV complexes is different from photoinduced ET in the U-shaped organic D-B-A system in aromatic solvents, where the inclusion of solvent molecules facilitates the ET (Kumar et al., 1996; Nadeau et al., 2003; Napper et al., 2002).

Contrarily, in hexafluorobenzene, there are no substantial changes in the spectra for 2^+ and 3^+, in comparison with the spectra in DCM (Figures 3B–3C). The IVCT bands are slightly blue-shifted, but the absorptions remain intense and the MLCT absorbances are also similar to those in DCM (Figures 3, S19, and S20). As is known, for fully delocalized species far beyond the Class II–III borderline, the IVCT absorption arises from the resonance of the valence electrons between the delocalized MOs (Brunschwig et al., 2002; D'Alessandro and Keene, 2006). A further increase of EC enlarges the orbital energy splitting, resulting in an increase of the "IVCT" energy (Tan et al., 2017). Therefore, the distinct optical behaviors for 2^+ and 3^+, in contrast to those in benzene, indicate that the EC is enhanced for the complexes in this nonpolar solvent (C_6F_6), consistent with the predictions from the dielectric continuum theory (Marcus and Sutin, 1985; Chen and Meyer, 1998). This is further confirmed in comparison with the spectral properties of the thienylene bridged analogues in hexafluorobenzene (Mallick et al., 2019), where the strong decoupling effects give rise to weak and broad IVCT absorptions.

Figures 3D–3F display the IVCT absorptions in a DCM-C_6H_6 mixed solvent that vary in energy and intensity as a function of the solvent ratio. For all three MV systems, increasing the benzene content constantly lowers the IVCT absorbance. In the solution with ≤60% C_6H_6, the band shape remains nearly unchanged. The band shape is varied notably as the benzene content reaches 80%, indicating that the C_6H_6 solvation
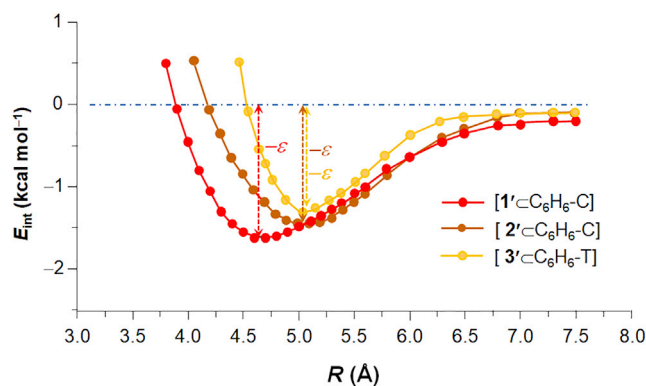
Figure 4. *ab initio* calculated nuclear PESs for the binary complex models
For each of the systems, the nuclear equilibrium (R_0) corresponds to the intermolecular distance between the complex bridge and the mass center of the included C_6H_6 molecule at the energy minimum.

mode is operative. The decoupling effect is also indicated by variation of the IVCT band symmetry. According to the two-state model (Brunschwig et al., 2002; D'Alessandro and Keene, 2006), increasing the extent of EC leads to an asymmetric IVCT band that is truncated at the low-energy side, an optical phenomenon known as "cut-off." The three MV complexes in different solvents show different "cut-off" areas (Table 1 and Table S7). For 1^+, the cut-off area is reduced from 28.1% in DCM to 16.9% (Table 1), as measured from the difference between the observed bandwidth at the half-height ($\Delta\nu_{1/2}$(exp)) and the Gaussian-shape simulated half-height bandwidth ($\Delta\nu_{1/2}$(simu)) (D'Alessandro and Keene, 2006; Tan et al., 2017). The large reduction of the cut-off area for 1^+, corresponding to decrease of band asymmetry in benzene, is consistent with the strong decoupling effect. Unlike 1^+ and 2^+, complex 3^+ presents similar cut-off areas in the two solvents (Table 1). Therefore, as a consequence of decoupling in benzene, the mixed-valency of 1^+ and 2^+ is changed from Classes II–III and Class III to Class II and II–III, respectively, whereas the very strongly coupled 3^+ remains in the same Robin–Day category, i.e., Class III (Table 1).

Intermolecular interaction energies of the supramolecular D-B-A systems

Energy minimization of the supramolecular structures for **1** and **2** capturing one C_6H_6 molecule in the crossing mode generated the space-filling models, namely [**1**$\subset$$C_6H_6$-C] and [**2**$\subset$$C_6H_6$-C], as shown in Figure 1. For **3**, which has no benzene molecule trapped in the crystal structure, two possible host–guest configuration modes, crossing and T-shape, are constructed for structural optimization, yielding the space-filling models [**3**$\subset$$C_6H_6$-C] and T-shaped [**3**$\subset$$C_6H_6$-T] (Figure 1C). In the latter, the C_6H_6 molecule in the cleft contacts the bridging ligand through one of the H atoms, similar to the T-shape benzene dimers (Hobza et al., 1996). Models [**1**$\subset$$C_6H_6$-C] and [**2**$\subset$$C_6H_6$-C] have the centroid distances 4.60 and 5.07 Å, respectively, consistent with the structural parameters for **1**$\subset$$C_6H_6$ and **2**$\subset$$C_6H_6$ (Figures 1A and 1B). For [**3**$\subset$$C_6H_6$-C], this distance is increased to 5.3 Å, longer than that for [**3**$\subset$$C_6H_6$-T] (5.0 Å), as seen in the benzene-ethene adducts (Ōki et al., 2000) and the T-shaped benzene dimers (Hobza et al., 1996; Lee et al., 2007), respectively. It is important to note that structural optimizations of the C_6F_6 binary complexes yield the space-filling models without a C_6F_6 molecule included in the cleft (Figure S21). This result is in agreement with the X-ray structures from single crystals grown in hexafluorobenzene that do not capture a C_6F_6 molecule in the cleft (Figure S9). Presumably, this is because the complex cavity does not complement geometrically and electrostatically the C_6F_6 molecule in the context of molecular recognition, thus showing the molecular signature of a "lock and key" relationship in supramolecular chemistry (Lehn, 2007).

To determine the intermolecular interaction energy (E_{int}), *ab initio* calculations using the CCSD(T) method together with the aug-cc-pVDZ basis set (Chalasinski and Szczesniak, 1994; Kaplan, 2006; Tsuzuki et al., 2002) were performed on the computational models of the binary complexes [**1'**$\subset$$C_6H_6$-C], [**2'**$\subset$$C_6H_6$-C], [**3'**$\subset$$C_6H_6$-C], and [**3'**$\subset$$C_6H_6$-T], for which the molecular structures (**1**, **2**, and **3**) are simplified as **1'**, **2'**, and **3'** by replacing the bulky *p*-isopropylphenyl groups on the DIppF ligands with hydrogen atoms. In these models, the complex core structures and the host–guest contacts agree with those in the associated space-filling models. For each system, as shown in Figures 4 and S22, E_{int} varies as a function of the intermolecular distance (R) equaling the mass center distance of the C_6H_6 molecule from the bridge of the Mo_2 dimer, generating the R-dependent potential energy surface (PES) with a global energy minimum at R_0. The

relaxed intermolecular interaction energies (E_{int}) are determined to be −1.62 kcal mol^{-1} for [$\mathbf{1'}\subset C_6H_6$-C], −1.45 kcal mol^{-1} for [$\mathbf{2'}\subset C_6H_6$-C], −1.30 kcal mol^{-1} for [$\mathbf{3'}\subset C_6H_6$-C], and −1.36 kcal mol^{-1} for [$\mathbf{3'}\subset C_6H_6$-T] (Figure 4). These E_{int} values are in excellent agreement with the calculated binding energies for benzene-ethene adducts (Ōki et al., 2000), for example, −1.637 kcal mol^{-1} for the crossing mode (C_{2v}), and −1.386 kcal mol^{-1} for the T-shape mode (C_{2v}) (Lee et al., 2007), and also comparable with the data for T-shaped benzene adducts or dimers (Hobza et al., 1996; Tsuzuki et al., 2002). For the series, the calculated binding energy decreases with S atoms being introduced stepwise, which explain the different crystal structures with and without capturing a C_6H_6 molecule in the cleft. Importantly, for these systems, the PES well depths (E_{int}) are more than twice of the thermal energy k_BT (≈ 0.6 kcal mol^{-1}), thereby yielding the supramolecular entities with stable equilibrium populations (Weinhold et al., 2005).

DFT calculations on the intermolecular orbital interactions

Single-point DFT calculations were performed on the computational models of unsolvated dimers $\mathbf{1'}$, $\mathbf{2'}$, and $\mathbf{3'}$ as well as the supramolecular models, [$\mathbf{1'}\subset C_6H_6$-C], [$\mathbf{2'}\subset C_6H_6$-C], [$\mathbf{3'}\subset C_6H_6$-C], and [$\mathbf{3'}\subset C_6H_6$-T]. For the Mo$_2$ dimers, the HOMO and HOMO-1 are formed in "antibonding" ($\delta - \delta$) and "bonding" ($\delta + \delta$) modes, respectively, in terms of the δ–δ interaction (Figures S23–S25). Models $\mathbf{1'}$ and $\mathbf{3'}$ have the smallest (3,145 cm^{-1}) and largest (4,920 cm^{-1}) HOMO-HOMO-1 energy gap (ΔE_{H-H-1}), corresponding to the weakest and strongest Mo$_2$-Mo$_2$ coupling (Tan et al., 2017; Xiao et al., 2013), respectively. The HOMO and HOMO-1 for the supramolecular models have the density unchanged, but energy splitting is reduced relative to the two MOs for the associated unsolvated model dimers (Figures S23–S25 and Table 1), showing the weakened "δ to δ" interaction, which provides theoretical evidence for the decoupling effects of the included benzene molecule. Remarkably, for the series, a decrease of the HOMO-HOMO-1 gap (ΔE_{H-H-1}) is quantitatively correlated to the blue-shifts of the IVCT band (ΔE_{IT}) in benzene (Table 1). For example, the largest ΔE_{H-H-1} decrease (0.07 eV) and the largest ΔE_{IT} (1,187 cm^{-1}) are found for [$\mathbf{1'}\subset C_6H_6$-C]. These results indicate implicitly that the inclusion of benzene molecule increases the reorganization energy of ET, and that the C_6H_6 molecule attenuates EC through orbital interactions. For the binary complex models, both the HOMO and LUMO energies increase, but small energy changes (0.02–0.06 eV) are found for the HOMO (Figures S23–S25). For both the unsolvated Mo$_2$ dimers and their C_6H_6 adducts, the HOMO-LUMO gaps calculated from the models are comparable with the MLCT energies in the spectra (Table S8), as seen in other dimeric complexes of Mo$_2$ (Tan et al., 2017; Xiao et al., 2013). The remarkable agreements between the computational results and experimental observations validate the singly solvated models for the MV complexes in benzene. The theoretical basis of single-point DFT calculations for the cationic radicals is the Koopmans theorem that states the one-electron Hamiltonian is transformed to a symmetrized basis of bonding (HOMO-1) and antibonding (HOMO) orbitals (Newton, 1991). Specifically, the transition energies for the radical cations are calculated using the "neutral in cation geometry" (NCG) method used in organic MV systems (Nelsen et al., 2005a, 2005b). This means, for example, that the calculated HOMO-1 and HOMO from the close-shell neutral molecule correspond to the SOMO and HOMO for the radical species in energy and density distribution of the states. For the strongly coupled Mo$_2$-Mo$_2$ MV systems (Tan et al., 2017), this approach yields results fully consistent with experimental observations, demonstrating that in the Class III system, the vibronic transition energy (IVCT) is determined by ΔE_{H-H-1} (Brunschwig et al., 2002; Newton, 1991). Therefore, in this study, the spectral data for the MV complexes in varied solvents are interpreted on the basis of single-point DFT computational results from the associated neutral models.

In the MO analysis, particular attention has been paid to HOMO-5 consisting of the π orbitals of the chelating atoms (E) (Figures 5A and 5B), thus being involved in LMCT transition (Figures S23–S25), when applicable. For $\mathbf{1'}$, the energy gaps from HOMO-5 to HOMO and HOMO-1 are 16,700 and 13,550 cm^{-1}, respectively, in good agreement with the LMCT absorption energies (16,330 and 14,740 cm^{-1}) in the spectra of $\mathbf{1^+}$ (Figure 3A and Table S6) and of the DAniF analogue in DCM (Tan et al., 2017). Observation of two LMCT bands in the spectrum implicates that the SOMO and HOMO of the MV species are resonant states that are close in energy owing to the interference of the benzene guest molecule. In the supramolecular models, this bridge-centered MO (HOMO-5 of $\mathbf{1'}$ or $\mathbf{2'}$) interacts selectively with the benzene HOMO (π_2). Orbital overlaps in π symmetry between them occur along the centroid connection between the complex bridge and the C_6H_6 ring, developing symmetric (low-energy) and asymmetric (high-energy) MOs for the supramolecule. For [$\mathbf{1'}\subset C_6H_6$-C], bonding orbital interactions produce HOMO-6 (asymmetric) and HOMO-7 (symmetric) separated by $\Delta E_{A-S} = 0.11$ eV (Figure 5A), and meanwhile, a pair of LUMOs, the LUMO+3 (out-of-phase) and LUMO+2 (in-phase) with $\Delta E_{A-S} = 0.12$ eV, is generated by mixing the LUMO+2 ($\mathbf{1'}$) and LUMO (π_5) (C_6H_6) (Figure 5B). Importantly, these MOs for the supramolecular entities are substantially different from HOMO-5 and LUMO+2 of $\mathbf{1'}$ (or $\mathbf{2'}$) with an
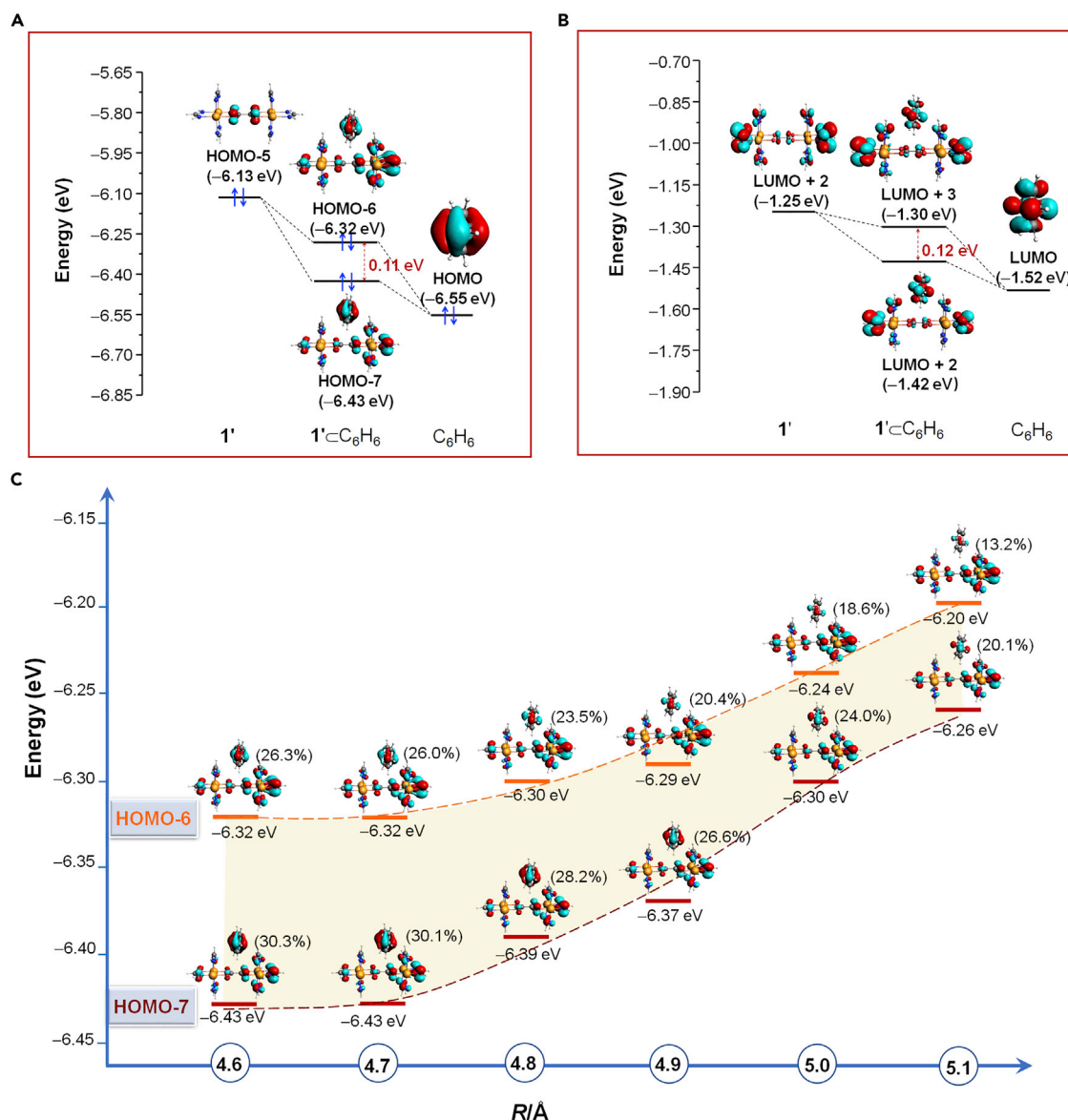
Figure 5. Diagrams of Intermolecular orbital interactions (isodensity value ± 0.03) between the complex and C_6H_6 molecule in the supramolecular systems [1'⊂C_6H_6-C]

(A) Interaction of HOMO-5 (1') with π_2 (C_6H_6) generates HOMO-6 and HOMO-7 with ΔE_{A-S} 0.11 eV for [1'⊂C_6H_6-C].

(B) Interaction of LUMO+2 (1') with π^* (C_6H_6) generates LUMO+3 and LUMO+2 with ΔE_{A-S} 0.12 eV for [1'⊂C_6H_6-C].

(C) Variations of density distribution and energy levels for the HOMO-6 and HOMO-7 for [1'⊂C_6H_6-C] as a function of intermolecular distance R (Å). The density contribution of the benzene orbital (π_2) to the MOs is shown by percentage in the parenthesis. The complete MO diagrams for the systems under investigation are presented in Figures S23–S25.

electron density of more than 25% on the encased benzene π orbital (Figure 5); surprisingly, there is no C_6H_6 density contributing to the other occupied MOs of the supramolecular complexes (Figure S23). Compared with HOMO-5 of 1', the filled bridge MOs of the benzene adduct decrease in energy by 0.19 (1,533 cm^{-1}) and 0.3 eV (2,420 cm^{-1}) (Figure 5A). Remarkably, in the spectra of 1$^+$ in benzene (Figure 3A), the LMCT bands are blue-shifted by ~ 2,000 cm^{-1}. For [2'⊂C_6H_6-C], the energy differences between the bridge orbital (HOMO-7) and the metal orbitals HOMO and HOMO-1 are 1.24 eV (10,000 cm^{-1}) and 1.73 eV (13,956 cm^{-1}) (Figure S24), respectively, in good agreement with the LMCT absorption at 12,650 cm^{-1} for 2$^+$ in benzene (Figure 3B). Inter-molecular orbital interactions may also lower the unoccupied orbital of the bridge (π^*), as shown in Figure 5B for 1', resulting in the decrease of the MLCT energy. The increase of the LMCT and decrease of MLCT energy is

representative of destructive and constructive interfering pathways, respectively, with respect of the donor-acceptor coupling (Troisi et al., 2004). Calculations show that for all supramolecular systems, the destructive pathway is dominant over the constructive one (Figures S23–S25). A computational study indicates that in the C-clamp D-B-A system, there are many solvent orbitals contributing to solvent-mediated coupling, and the constructive paths play the role in facilitating the photoinduced ET (Troisi et al., 2004). Clearly, electronic decoupling of the mixed-valence complexes in benzene is the consequence of including a C_6H_6 molecule in the cleft that electronically interacts with the bridge moiety of Mo_2 dimer. Overall, it is evidenced that the solute–solvent orbital interactions enable mediation of EC by manipulating the superexchange paths (Liu et al., 2013; McConnell, 1961).

The intermolecular orbital overlaps in the supramolecular systems are reminiscent of the intramolecular orbital interactions occurring between atoms that are not directly connected, described as through-space interatomic orbital interaction by Hoffmann (Hoffmann, 1971), except for the nuclear dynamics. The splitting in energy between the two resultant supramolecular orbitals (Figures 5A and 5B), $\Delta E_{A\text{-}S}$, reflects the strength of the intermolecular orbital interactions, just as the $\Delta E_{H\text{-}H\text{-}1}$ magnitude measures the extent of the intramolecular Mo_2 to Mo_2 coupling through the covalent bridge (Tan et al., 2017; Xiao et al., 2013). For [$\mathbf{1}'{\subset}C_6H_6$-C] (Figure 5A), $\Delta E_{A\text{-}S}$ of 0.11 eV is much larger than the values for the weakly decoupled systems (~0.05 eV) (Figures S24, and S25). It should be noted that whereas the resulting HOMO-6 and HOMO-7 have the energy levels lower than HOMO-5 of $\mathbf{1}'$, the energies for all other filled MOs increase (Table S10), which is ascribable to the Pauli repulsive exchange energy. Significantly, the orbital interactions between molecules satisfy the symmetry, energy, and directionality requirements; quantum mechanically in analogy to interatomic orbital interaction.

Coupling of the electronic states with the intermolecular nuclear configuration

For each system, the MOs (Figure S23, S24 and S25) for the supramolecular model are coded by the geometric topology of the intermolecular binding. In the strongly interacting system, [$\mathbf{1}'{\subset}C_6H_6$-C], in addition to mixing of π electron clouds between the bridging atoms and C_6H_6, orbital interactions also take place on the side where the host–guest contacts are in short distances, generating the asymmetric HOMO-6 and HOMO-7. In [$\mathbf{2}'{\subset}C_6H_6$-C] (Figure S24B), the two bridge MOs are less asymmetric owing to the relatively large host–guest separations that yield weak intermolecular interactions. Significantly, the small differences in geometric topology between the supramolecular structures are magnified in the solute–solvent orbital interactions, with respect to the density, symmetry, and directionality, presenting the molecular signatures of intermolecular orbital interactions at an atomic level (Figures 5A, 5B, S23, S24, and S25).

For [$\mathbf{1}'{\subset}C_6H_6$-C], the intermolecular nuclear dynamics that affect the intramolecular electronic interaction were modeled with progressively increasing the centroid distance (R) starting from R_0 (4.6 Å). As shown in Figure 5C, strong intermolecular orbital interactions occur at the nuclear equilibrium (R_0), as indicated by the largest contribution of C_6H_6 (>25%) on HOMO-6 and HOMO-7 and the largest energy splitting ($\Delta E_{A\text{-}S}$) between them; both of the quantities decrease constantly with an increase of R, accompanied by an increase of the potential energy (E_{int}). By changing R from 4.7 to 4.9 Å, the HOMO-7 energy is increased by 0.06 eV. For the next two successive increments of 0.1 Å of R, the orbital energy is raised by 0.07 and 0.04 eV. Plotting the MO energies against the intermolecular nuclear distance shows variation of the attractive electronic energies along the intermolecular nuclear configuration coordinate. This plot (Figure 5C) can be viewed as the electronic PES for solute–solvent complexation, which has a potential minimum at the sum of van der Waals radii, corresponding to the nuclear PES (Figure 4). Therefore, it is evidenced that in the supramolecular system, the intramolecular vibronic transition (Frank–Condon transition) is coupled with the intermolecular nuclear motion. Population of the electronic states in the vicinity of the nuclear equilibrium accounts for the coupling fluctuations with nuclear dynamics of the solvated C_6H_6 molecule (Troisi et al., 2004). This may lead us to view the intermolecular nuclei–electron interactions and the dynamics under the framework of Born–Oppenheimer approximation (Born and Huang, 1968; Whetten et al., 1985).

Quantum mechanics of the intermolecular electronic interactions

Figure 5 shows that orbital interactions between the host and guest can be described by symmetry adapted linear combination (SALC) of the molecular (fragment) orbitals,

$$\psi_S = N(\Phi_h + \Phi_g) \tag{Equation 1}$$
$$\psi_A = N(\Phi_h - \Phi_g) \tag{Equation 2}$$

where Ψ_S and Ψ_A are the bonding (symmetric) and antibonding (asymmetric) MOs, for example, HOMO-7 and HOMO-6 in [$\mathbf{1}' \subset C_6H_6$-C], respectively, and φ_h and φ_g represent the reacting MOs from the host and guest, that is, HOMO-5 of the complex and HOMO (π_2) of C_6H_6. SALC of the two MOs ensures the antisymmetric character of the resultant MOs for the binary complex, in terms of electron exchange, to satisfy the *Pauli's exclusion principle* (Jeziorski et al., 1994; Kaplan, 2006). Therefore, in this system, we estimated the Pauli exchange energy ($\Delta E_{Pauli} > 0$) from the overall energy increase of the filled MOs and the orbital interaction energy ΔE_{Orb} (<0) from the energy decrease of the bridge MO, which measures the intermolecular interaction strength. Borrowing the concept from the supramolecular MP perturbation theory (Jeziorski et al., 1994; Kaplan, 2006; Weinhold et al., 2005), electronic interaction energy ($E_{electro}$) resulting from orbital interactions can be approximated from

$$E_{electro} = E_{AB} - (E_A + E_B) \tag{Equation 3}$$

where E_{AB} is the sum of energies of all occupied MOs for the binary complex, E_A is the total energy of the occupied MOs for the host complex, and E_B is the energy of the benzene reacting orbital, i.e., HOMO (π_2). Here $E_{electro}$ corresponds to the first-order exchange energy of the perturbation theory, E_{exch} (Kaplan, 2006). For [$\mathbf{1}' \subset C_6H_6$-C] and [$\mathbf{2}' \subset C_6H_6$-C], as listed in Table S10, $E_{electro} = 15.91$ (0.69 eV) and 18.21 kcal mol^{-1} (0.79 eV), respectively. For the two C_6H_6 adduct models of **3**, [$\mathbf{3}' \subset C_6H_6$-C] and [$\mathbf{3}' \subset C_6H_6$-T], the electronic interaction energies are determined to be 1.19 and 0.65 eV, respectively (Table S10). This electronic term of intermolecular interaction energy is the sum of ΔE_{Pauli} and ΔE_{Orb}, and thus,

$$\Delta E_{Pauli} = E_{electro} - \Delta E_{Ord} \tag{Equation 4}$$

For [$\mathbf{1}' \subset C_6H_6$-C], $\Delta E_{Orb} = -0.24$ eV (-5.53 kcal mol^{-1}), calculated by averaging the energy decreases of HOMO-6 and HOMO-7 relative to HOMO-5 of **1'** (Table S10); then, ΔE_{Pauli} is determined to be 0.93 eV (21.44 kcal mol^{-1}). The ΔE_{Pauli} and ΔE_{Orb} values for [$\mathbf{1}' \subset C_6H_6$-C] are comparable with those for some boron-trihalide Lewis acid-base complexes that define the so-called *triel bonds* (Grabowski, 2018). Model [$\mathbf{3}' \subset C_6H_6$-C] with the largest intermolecular centroid distance (5.3 Å) exhibits weak intermolecular orbital interactions with small ΔE_{Orb} (-0.06 eV), but unreasonably high Pauli exchange energy (Table S10, $\Delta E_{Pauli} = 1.25$ eV); therefore, this solvation model of **3** should be ruled out. The solvation model [$\mathbf{3}' \subset C_6H_6$-T] is favorable because the fully thiolated bridge eliminates the O···H-C interaction in the crossing mode, and, on the other hand, the increased π electron density on the C−C bridge enhances the π···H-C interaction for the T geometry (Figure 3), which gives the energy parameters (E_{int}, ΔE_{Pauli} and ΔE_{Orb}) in acceptable magnitudes (Table S10).

DISCUSSIONS

Integration of the molar extinction coefficient (ε) over the frequency (ν) of the absorbed photons gives rise to the integrated spectral band shape (Barbara et al., 1996; Chen and Meyer, 1998; Heckmann and Lambert, 2012),

$$\int \varepsilon(\nu) d\nu = \frac{2000 N_A \pi^2}{3\varepsilon_0 \ln 10} \frac{(n^2+2)^2}{9n} \overrightarrow{\mu}_{ab}^2 \times \left(\frac{1}{4\pi hc\lambda_0 k_B T} \right)^{1/2} FC \tag{Equation 6}$$

where N_A is the Avogadro constant, h is the Planck constant, n is the refractive index of the solvent, ε_0 is the dielectric constant of the solvent, and c is the speed of light. In Equation (6), μ_{12} is the transition dipole moment and FC is the Frank–Condon factor weighted by the density of nuclear states in the electronic ground state of the reactant that dominates the vibronic transition (Barbara et al., 1996). Accordingly, for each complex system, the integrated absorption band area $\int \varepsilon(\nu) d\nu$ was determined from the spectrum that reflects the impact of the nuclear dynamics on the Frank–Condon (vibronic) transition. In DCM and C_6F_6, the MV complexes show similar absorption areas for both the electronic and IVCT transitions (Figures 3A–3C and Table S7). In contrast, whereas the total MLCT and LMCT band areas remain almost constant in DCM and C_6H_6, the IVCT band area in benzene decreases by a half for $\mathbf{1}^+$, or by 85% (or more) for $\mathbf{2}^+$ and $\mathbf{3}^+$ (Figures 3A–3C and Table S7). According to the Beer–Lambert law, the molar extinction coefficient (ε) is inversely related to the concentration. The great decrease of ε_{IT} for the same complex in benzene indicates that the effective concentration of the species that conducts the charge transfer is much lower than the initial concentration of the MV complex. Following in this vein, we may further infer that in benzene, only part of the complex molecules absorbs the near-IR photons for intervalence transition, or, in other words, that benzene molecules suppress the donor-acceptor EC and ET.

On this basis, in the context of the Frank–Condon factor (Barbara et al., 1996; Heckmann and Lambert, 2012), we separate the stoichiometric complex molecules in benzene solution into two subsets. Those

undergoing IVCT are the supramolecules in the nuclear ground state or in the vicinity of nuclear equilibrium, namely $\{[Mo_2\text{-}Mo_2] \subset C_6H_6\}$, whereas the IVCT silent MV molecules are in the nuclear non-equilibrium states that are highly energetic, dynamic, and short-lived, termed as $\{[Mo_2\text{-}Mo_2] | C_6H_6\}$. In other words, solute molecules tightly contacting with the solvent molecule experience strong intermolecular interaction, which are decoupled by intermolecular orbital interaction. For the short-lived entities $\{[Mo_2\text{-}Mo_2] | C_6H_6\}$, the frequently shuttling C_6H_6 molecule disables completely the charge transfer or the donor-acceptor vibronic transition by electronically disturbing the bridging orbital of the MV complex, leading to the simultaneous breakdown of the Born–Oppenheimer approximation (Whetten et al., 1985) and the Condon approximation (Toutounji and Ratner, 2000; Troisi et al., 2004). Our observations and analyses are in full agreement with the results of molecular dynamics study (Troisi et al., 2004) on the solvent-mediated C-clamp system (Napper et al., 2002). It predicates that a small subset of solute–solvent configurations dominates the solvent-mediated coupling (Troisi et al., 2004). The calculated timescale of ~0.1 ps for solvent-induced coupling fluctuation (Troisi et al., 2004) is comparable with the thermal ET rate limit for Class II–III MV systems in solvent medium (Lear et al., 2007; Liu et al., 2013) with the average nuclear vibrational transition frequency (v_n), i.e., $v_n = 5 \times 10^{12}\,s^{-1}$ (Creutz, 1983; Zhu et al., 2021). In our systems, the observed blue-shift of the IVCT band and suppression of the intervalence transition manifest the coupling fluctuations (Troisi et al., 2004) that are accounted by the two subsets differing in solute–solvent nuclear configuration. Obviously, the ratio of $\{[Mo_2\text{-}Mo_2] \subset C_6H_6\}:\{[Mo_2\text{-}Mo_2] | C_6H_6\}$ for a given system is correlated to the population of the supramolecular entities defined by the coordinate of the nuclear configuration (Figure 4). For $[1^+ \subset C_6H_6\text{-}C]$, the deep well of the nuclear PES accounts for the large fraction of $\{[Mo_2\text{-}Mo_2] \subset C_6H_6\}$ and vice versa, in the cases of 2^+ and 3^+ in benzene. This means that of the three systems in benzene, 1^+ has more solvated molecules that suffer stronger decoupling. This speculation explains well the large blue-shift (1,187 cm^{-1}) and the high intensity (($\varepsilon_{IT} = 2,209\,cm^{-1}$) of the IVCT absorption for 1^+ in benzene, relative to 2^+ and 3^+ (vide supra). In contrast, for system 3^+, there is a small fraction of $\{[Mo_2\text{-}Mo_2] \subset C_6H_6\}$, the benzene molecule in $[3^+ \subset C_6H_6\text{-}T]$ is more dynamic, but the intermolecular electronic interaction is weak owing to the small interaction energy (Figure 4). These factors bring distinct IVCT features to 3^+ (in benzene), such as an only small increase of transition energy (188 cm^{-1}), lower symmetry (cut-off increase), and low intensity ($\varepsilon_{IT} = 1,500\,cm^{-1}$) (Table 1). The imaginable picture for the decoupling effect is that a C_6H_6 molecule flashes in and out the cleft between the two Mo_2 units, disturbing the electronic state of the D-B-A molecule by interfering with the related MO, as shown in Figure 6.

Collectively, we have shown that strongly coupled mixed-valence D-B-A complexes are decoupled in benzene and the intramolecular electron transfer is gated by intermolecular interaction with a C_6H_6 molecule captured in the cleft between the D and A units. The substantial orbital interactions between the complex and the solvating benzene molecule are attributed to suitable matching of the reacting MOs in symmetry and energy, in analogy to interatomic orbital interaction. This work demonstrates intermolecular electronic interactions in the van der Waals distance limit and the underlying effects, showing the potential of supramolecular strategy leading to innovative complex matters and "smart materials" and providing guidance in elucidating the intermolecular interactions in biological systems.

Limitations of the study

In this study, intermolecular interaction energies were calculated for the simplified supramolecular models using coupled cluster CCSD(T) method. We have not performed other methods like HF, MP2 for comparison because the computational results are reasonable and supportive to the experimental data. The speculation that two subsets of stoichiometric complexes exist in benzene solution, namely $\{[Mo_2\text{-}Mo_2] \subset C_6H_6\}$ and IVCT silent $\{[Mo_2\text{-}Mo_2] | C_6H_6\}$, is given on the basis of optical analyses and theoretical predictions from literature, but the two supramolecular species are not detected directly owing to the dynamic nature of the system.

STAR★METHODS

Detailed methods are provided in the online version of this paper and include the following:

- KEY RESOURCES TABLE
- RESOURCE AVAILABILITY
  - Lead contact
  - Materials availability
  - Data and code availability
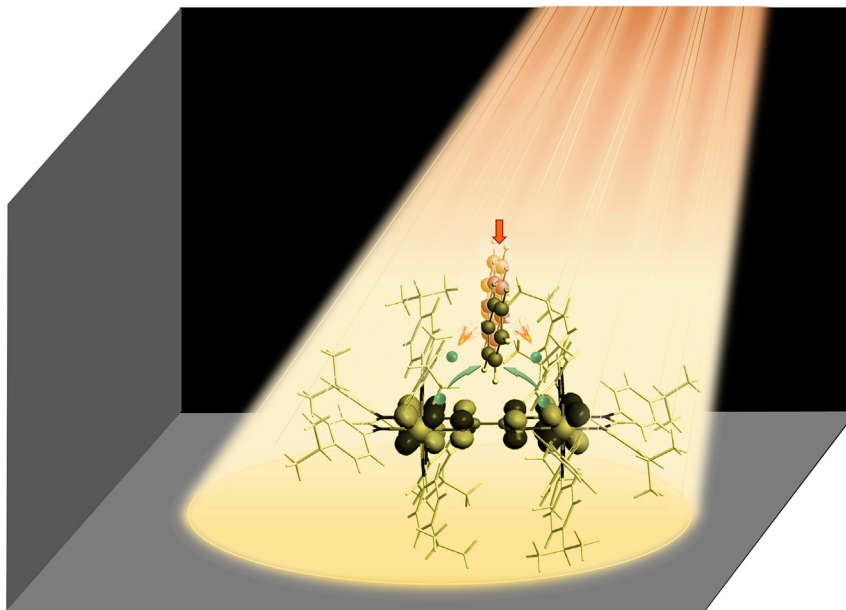- EXPERIMENTAL MODEL AND SUBJECT DETAILS

Figure 6. A pictorial description of mediation of a single solvating C_6H_6 molecule on optical electron transfer in the supramolecular system [1⊂C_6H_6-C]

According to the optical and the DFT calculation results, electron coupling and electron transfer between the two Mo_2 centers are literally blocked by the encapsulated benzene molecule in the cleft by interfering with the superexchange pathway.

- METHOD DETAILS
  - Synthesis of complex 1
  - General synthesis of complexes 2 and 3
  - Electrochemistry
  - X-Ray structural determination
  - EPR spectroscopy
  - Spectroscopic measurements
  - DFT calculations
- QUANTIFICATION AND STATISTICAL ANALYSIS
- ADDITIONAL RESOURCES

SUPPLEMENTAL INFORMATION

Supplemental information can be found online at https://doi.org/10.1016/j.isci.2022.104365.

AUTHOR CONTRIBUTIONS

C.Y.L. conceived this project and designed the experiments and worked on the manuscript. S.M. performed experimental works, theoretical calculations and prepared the supplementary information. Y.Z. and M.M. worked on crystal growth, crystallographic data collection, refinement and analysis for molecular structural determination, and assisted in manuscript preparation. X.C. carried out the major experimental work and spectroscopic data analysis. Y.N.T., L.C., Y.Q., Z.C.H., T.C., and G.Y.Z. were involved in experimental investigations.

DECLARATION OF INTERESTS

The authors declare no competing interests.

REFERENCES

Arunan, E., Desiraju, G.R., Klein, R.A., Sadlej, J., Scheiner, S., Alkorta, I., Clary, D.C., Crabtree, R.H., Dannenberg, J.J., Hobza, P., et al. (2011). Definition of the hydrogen bond (IUPAC Recommendations 2011). Pure Appl. Chem. 83, 1637–1641. https://doi.org/10.1351/pac-rec-10-01-02.

Barbara, P.F., Meyer, T.J., and Ratner, M.A. (1996). Contemporary issues in electron transfer research. J. Phys. Chem. 100, 13148–13168. https://doi.org/10.1021/jp9605663.

Becke, A.D. (1988). Density-functional exchange-energy approximation with correct asymptotic behavior. Phys. Rev. 38, 3098–3100. https://doi.org/10.1103/physreva.38.3098.

Biasin, E., Fox, Z.W., Andersen, A., Ledbetter, K., Kjær, K.S., Alonso-Mori, R., Carlstad, J.M., Chollet, M., Gaynor, J.D., Glownia, J.M., et al. (2021). Direct observation of coherent femtosecond solvent reorganization coupled to intramolecular electron transfer. Nat. Chem. 13, 343–349. https://doi.org/10.1038/s41557-020-00629-3.

Born, M., and Huang, K. (1968). Dynamical Theory of Crystal Lattices (Oxford University Press).

Brunschwig, B.S., Creutz, C., and Sutin, N. (2002). Optical transitions of symmetrical mixed-valence systems in the Class II–III transition regimeElectronic supplementary information (ESI) is available: derivation of eqn. (39c), table summarizing the relationships between band maxima and band widths predicted by the two-state model and table of spectral properties of mixed-valence ruthenium(II)/(III) bridged by pyrazine and dicyanamide. See http://www.rsc.org/suppdata/cs/b0/b008034i/. Chem. Soc. Rev. 31, 168–184. https://doi.org/10.1039/b008034i.

Chalasinski, G., and Szczesniak, M.M. (1994). Origins of structure and energetics of van der Waals clusters from ab initio calculations. Chem. Rev. 94, 1723–1765. https://doi.org/10.1021/cr00031a001.

Chen, P.Y., and Meyer, T.J. (1998). Medium effects on charge transfer in metal complexes. Chem. Rev. 98, 1439–1478. https://doi.org/10.1021/cr941180w.

Hunter, C.A. (2004). Quantifying intermolecular interactions: guidelines for the molecular recognition toolbox. Angew. Chem. Int. Ed. 43, 5310–5324. https://doi.org/10.1002/anie.200301739.

Cotton, F.A., and Nocera, D.G. (2000). The whole story of the two-electron bond, with the δ bond as a paradigm. Acc. Chem. Res. 33, 483–490. https://doi.org/10.1021/ar980116o.

Cotton, F.A., Liu, C.Y., Murillo, C.A., Villagrán, D., and Wang, X. (2003). Modifying electronic communication in dimolybdenum units by linkage isomers of bridged oxamidate dianions. J. Am. Chem. Soc. 125, 13564–13575. https://doi.org/10.1021/ja036884e.

Creutz, C. (1983). Mixed-valence-complexes-of d5-d6-metal-centers. Prog. Inorg. Chem. 30, 1–73. https://doi.org/10.1002/9780470166314.ch1.

Crutchley, R.J. (1994). Intervalence charge transfer and electron exchange studies of dinuclear ruthenium complexes. Adv. Inorg. Chem. 41, 273–325. https://doi.org/10.1016/s0898-8838(08)60174-9.

CrysAlis RED, version 1.171.31.7; Oxford Diffraction Ltd, Abington, U.K., 2006

D'Alessandro, D.M., and Keene, F.R. (2006). Current trends and future challenges in the experimental, theoretical and computational analysis of intervalence charge transfer (IVCT) transitions. Chem. Soc. Rev. 35, 424–440. https://doi.org/10.1039/b514590m.

Eichkorn, K., Treutler, O., Ohm, H., Haser, M., and Ahlrichs, R. (1995). Auxiliary basis sets to approximate Coulomb potentials. Chem. Phys. Lett. 240, 283–290. https://doi.org/10.1016/0009-2614(95)00621-a.

Eichkorn, K., Weigend, F., Treutler, O., and Ahlrichs, R. (1997). Auxiliary basis sets for main row atoms and transition metals and their use to approximate Coulomb potentials. Theor. Chem. Acc. 97, 119–124. https://doi.org/10.1007/s002140050244.

Grabowski, S.J. (2011). What is the covalency of hydrogen bonding. Chem. Rev. 111, 2597–2625. https://doi.org/10.1021/cr800346f.

Grabowski, S.J. (2018). Two faces of triel bonds in boron trihalide complexes. J. Comput. Chem. 39, 472–480. https://doi.org/10.1002/jcc.25056.

Heckmann, A., and Lambert, C. (2012). Organic mixed-valence compounds: a Playground for electrons and holes. Angew. Chem. Int. Ed. 51, 326–392. https://doi.org/10.1002/anie.201100944.

Hobza, P., Selzle, H.L., and Schlag, E.W. (1996). Potential energy surface for the benzene dimer. Results of ab Initio CCSD(T) calculations show two nearly isoenergetic structures: T-shaped and parallel-displaced. J. Phys. Chem. 100, 18790–18794. https://doi.org/10.1021/jp961239y.

Hoffmann, R. (1971). Interaction of orbitals through space and through bonds. Acc. Chem. Res. 4, 1–9. https://doi.org/10.1021/ar50037a001.

Hush, N.S. (1967). Intervalence-transfer absorption. Part 2. Theoretical considerations and spectroscopic data. Prog. Inorg. Chem. 8, 391–444. https://doi.org/10.1002/9780470166093.ch7.

Isaacs, E.D., Shukla, A., Platzman, P.M., Hamann, D.R., Barbiellini, B., and Tulk, C.A. (1999). Covalency of the hydrogen bond in ice: a direct X-ray measurement. Phys. Rev. Lett. 82, 600–603. https://doi.org/10.1103/physrevlett.82.600.

Jeziorski, B., Moszynski, R., and Szalewicz, K. (1994). Perturbation theory approach to intermolecular potential energy surfaces of van der Waals complexes. Chem. Rev. 94, 1887–1930. https://doi.org/10.1021/cr00031a008.

Jurecka, P., Sponer, J., Cerny, J., and Hobza, P. (2006). Benchmark database of accurate (MP2 and CCSD(T) complete basis set limit) interaction energies of small model complexes, DNA base pairs, and amino acid pairs. Phys. Chem. Chem. Phys. 8, 1985–1993. https://doi.org/10.1039/b600027d.

Kaplan, I.G. (2006). Intermolecular Interactions: Physical Picture, Computational Methods and Model Potentials (John Wiley & Sons).

Kellett, C.W., Kennepohl, P., and Berlinguette, C.P. (2020). π covalency in the halogen bond. Nat. Commun. 11, 3310. https://doi.org/10.1038/s41467-020-17122-7.

Kumar, K., Lin, Z., Waldeck, D.H., and Zimmt, M.B. (1996). Electronic coupling in C-Clamp-Shaped molecules: solvent-mediated superexchange pathways. J. Am. Chem. Soc. 118, 243–244. https://doi.org/10.1021/ja952999+.

Lear, B.J., and Kubiak, C.P. (2007). Origins of cooperative noncovalent host-guest chemistry in mixed valence complexes. J. Phys. Chem. B 111, 6766–6771. https://doi.org/10.1021/jp068964l.

Lear, B.J., Glover, S.D., Salsman, J.C., Londergan, C.H., and Kubiak, C.P. (2007). Solvent dynamical control of ultrafast ground state electron transfer: Implications for Class II-III mixed valency. J. Am. Chem. Soc. 129, 12772–12779. https://doi.org/10.1021/ja072653m.

Lee, E.C., Kim, D., Jurecka, P., Tarakeshwar, P., Hobza, P., and Kim, K.S. (2007). Understanding of assembly phenomena by aromatic-aromatic interactions: benzene dimer and the substituted systems. J. Phys. Chem. A. 111, 3446–3457. https://doi.org/10.1021/jp068635t.

Lehn, J.-M. (2002). Toward self-organization and complex matter. Science 295, 2400–2403. https://doi.org/10.1126/science.1071063.

Lehn, J.-M. (2007). From supramolecular chemistry towards constitutional dynamic chemistry and adaptive chemistry. Chem. Soc. Rev. 38, 151–160. https://doi.org/10.1002/chin.200720232.

Lin, C., Protasiewicz, J.D., Smith, E.T., and Ren, T. (1996). Linear free energy relationships in dinuclear compounds. 2. Inductive redox tuning via remote substituents in quadruply bonded dimolybdenum compounds. Inorg. Chem. 35, 6422–6428. https://doi.org/10.1021/ic960555o.

Liu, C.Y., Xiao, X., Meng, M., Zhang, Y., and Han, M.J. (2013). Spectroscopic study of δ electron transfer between two covalently bonded dimolybdenum units via a conjugated bridge: adequate complex models to test the existing theories for electronic

coupling. J. Phys. Chem. C *117*, 19859–19865. https://doi.org/10.1021/jp406261w.

Mallick, S., Cao, L., Chen, X., Zhou, J.P., Qin, Y., Wang, G.Y., Wu, Y.Y., Meng, M., Zhu, G.Y., Tan, Y.N., and Cheng, T. (2019). Mediation of electron transfer by quadrupolar interactions: the constitutional, electronic, and energetic complementarities in supramolecular chemistry. iScience *22*, 269–287. https://doi.org/10.1016/j.isci.2019.11.020.

Marcus, R.A., and Sutin, N. (1985). Electron transfers in chemistry and biology. Biochimi. Biophys. Acta *811*, 265–322. https://doi.org/10.1016/0304-4173(85)90014-x.

McConnell, H.M. (1961). Intramolecular charge transfer in aromatic free radicals. J. Chem. Phys. *35*, 508–515. https://doi.org/10.1063/1.1731961.

Meyer, E.A., Castellano, R.K., and Diederich, F. (2003). Interactions with aromatic rings in chemical and biological recognition. Angew. Chem. Int. Ed. *34*, 1210–1250. https://doi.org/10.1002/chin.200322285.

Nadeau, J.M., Liu, M., Waldeck, D.H., and Zimmt, M.B. (2003). Hole transfer in a C-shaped molecule: conformational freedom versus solvent-mediated coupling. J. Am. Chem. Soc. *125*, 15964–15973. https://doi.org/10.1021/ja0372917.

Napper, A.M., Head, N.J., Oliver, A.M., Shephard, M.J., Paddon-Row, M.N., Read, I., and Waldeck, D.H. (2002). Use of U-shaped donor-bridge-acceptor molecules to study electron tunneling through nonbonded contacts. J. Am. Chem. Soc. *124*, 10171–10181. https://doi.org/10.1021/ja025683s.

Neese, F. (2003). An improvement of the resolution of the identity approximation for the formation of the Coulomb matrix. J. Comput. Chem. *24*, 1740–1747. https://doi.org/10.1002/jcc.10318.

Neese, F. (2012). The ORCA program system. Wires Comput. Mol. Sci. *2*, 73–78. https://doi.org/10.1002/wcms.81.

Nelsen, S.F., Konradsson, A.E., and Telo, J.P. (2005a). Pseudo-para-dinitro[2.2]paracyclophane radical anion, a mixed-valence system Poised on the Class II/Class III borderline. J. Am. Chem. Soc. *127*, 920–925. https://doi.org/10.1021/ja0441920.

Nelsen, S.F., Weaver, M.N., Zink, J.I., and Telo, J.P. (2005b). Optical spectra of delocalized dinitroaromatic radical anions revisited. J. Am. Chem. Soc. *127*, 10611–10622. https://doi.org/10.1021/ja051178u.

Newton, M.D. (1991). Quantum chemical Probes of electron-transfer kinetics: the nature of donor-acceptor interactions. Chem. Rev. *91*, 767–792. https://doi.org/10.1021/cr00005a007.

Ōki, M., Takano, S., and Toyota, S. (2000). Benzene-ethene interactions as studied by ab initio calculations. Bull. Chem. Soc. Jpn. *73*, 2221–2230. https://doi.org/10.1246/bcsj.73.2221.

Pantazis, D.A., Chen, X.Y., Landis, C.R., and Neese, F. (2008). All-electron scalar relativistic basis sets for third-Row transition metal atoms. J. Chem. Theor. Comput. *4*, 908–919. https://doi.org/10.1021/ct800047t.

Perdew, J.P. (1986). Density-functional approximation for the correlation energy of the inhomogeneous electron gas. Phys. Rev. B: Condens. Matter Mater. Phys. *33*, 8822–8824. https://doi.org/10.1103/physrevb.33.8822.

Politzer, P., Murray, J.S., and Clark, T. (2015). Mathematical modeling and physical reality in noncovalent interactions. J. Mol. Model. *21*, 52. https://doi.org/10.1007/s00894-015-2585-5.

Rezac, J., and Hobza, P. (2013). Describing noncovalent interactions beyond the common approximations: how accurate is the "Gold Standard," CCSD(T) at the complete basis set limit? J. Chem. Theor. Comput. *9*, 2151–2155. https://doi.org/10.1021/ct400057w.

Richardson, D.E., and Taube, H. (1981). Determination of $E_2^0 - E_1^0$ in multistep charge transfer by stationary-electrode pulse and cyclic voltammetry: application to binuclear ruthenium ammines. Inorg. Chem. *20*, 1278–1285. https://doi.org/10.1021/ic50218a062.

Robin, M.B., and Day, P. (1967). Mixed valence chemistry-a survey and classification. Adv. Inorg. Chem. Radiochem. *9*, 247–422. https://doi.org/10.1016/s0065-2792(08)60179-x.

Schafer, A., Horn, H., and Ahlrichs, R. (1992). Fully optimized contracted Gaussian basis sets for atoms Li to Kr. J. Chem. Phys. *97*, 2571–2577. https://doi.org/10.1063/1.463096.

Sheldrick, G.M. (2000). SHELXTL,version 6.12 (Bruker Analytical X-ray Systems, Inc).

Simova, L., Rezac, J., and Hobza, P. (2013). Convergence of the interaction energies in noncovalent complexes in the coupled-cluster methods up to full configuration interaction. J. Chem. Theor. Comput. *9*, 3420–3428. https://doi.org/10.1021/ct4002762.

Tan, Y.N., Cheng, T., Meng, M., Zhang, Y.Y., Liu, C.Y., Sun, M.F., and Low, P.J. (2017). Optical behaviors and electronic properties of Mo_2–Mo_2 mixed-valence complexes within or beyond the Class III regime: testing the limits of the two-state model. J. Phys. Chem. C *121*, 27860–27873. https://doi.org/10.1021/acs.jpcc.7b11082.

Tatko, C.D., and Waters, M.L. (2002). Selective aromatic interactions in β-hairpin Peptides. J. Am. Chem. Soc. *124*, 9372–9373. https://doi.org/10.1021/ja0262481.

Thomas, A., Meurisse, R., and Brasseur, R. (2002). Aromatic side-chain interactions in proteins. II. Near- and far-sequence Phe-X pairs. Proteins *48*, 635–644. https://doi.org/10.1002/prot.10191.

Tkachov, R., Stepien, L., Roch, A., Komber, H., Hennersdorf, F., Weigand, J.J., Bauer, I., Kiriy, A., and Leyens, C. (2017). Facile synthesis of potassium tetrathiooxalate — the "true" monomer for the preparation of electron-conductive poly(nickelethylenetetrathiolate).

Tetrahedron *73*, 2250–2254. https://doi.org/10.1016/j.tet.2017.03.010.

Toutounji, M.M., and Ratner, M.A. (2000). Testing the Condon approximation for electron transfer via the mulliken-hush model. J. Chem. Phys. A. *104*, 8566–8569. https://doi.org/10.1021/jp001271z.

Troisi, A., Ratner, M.A., and Zimmt, M.B. (2004). Dynamic nature of the intramolecular electronic coupling mediated by a solvent molecule: a computational study. J. Am. Chem. Soc. *126*, 2215–2224. https://doi.org/10.1021/ja038905a.

Tsuzuki, S., Honda, K., Uchimaru, T., Mikami, M., and Tanabe, K. (2000). The magnitude of the CH/π interaction between benzene and some model hydrocarbons. J. Am. Chem. Soc. *122*, 3746–3753. https://doi.org/10.1021/ja993972j.

Tsuzuki, S., Honda, K., Uchimaru, T., Mikami, M., and Tanabe, K. (2002). Origin of attraction and directionality of the π/π Interaction: model chemistry calculations of benzene dimer interaction. J. Am. Chem. Soc. *124*, 104–112. https://doi.org/10.1021/ja0105212.

Weigend, F., and Ahlrichs, R. (2005). Balanced basis sets of split valence, triple zeta valence and quadruple zeta valence quality for H to Rn: design and assessment of accuracy. Phys. Chem. Chem. Phys. *7*, 3297–3305. https://doi.org/10.1039/b508541a.

Weinhold, F., Landis, C.R., and Valency, B.A. (2005). Natural Bond Orbital Donor-Acceptor Perspective (University of Wisconsin), p. 317.

Whetten, R.L., Ezra, G.S., and Grant, E.R. (1985). Molecular dynamics beyond the adiabatic approximation: new experiments and theory. Ann. Rev. Phys. Chem. *36*, 277–320. https://doi.org/10.1146/annurev.pc.36.100185.001425.

Widmer, D.R., and Schwartz, B.J. (2018). Solvents can control solute molecular identity. Nat. Chem. *10*, 910–916. https://doi.org/10.1038/s41557-018-0066-z.

Wu, Y.Y., Meng, M., Wang, G.Y., Feng, P., and Liu, C.Y. (2017). Optically probing the localized to delocalized transition in Mo_2–Mo_2 mixed-valence systems. Chem. Commun. *53*, 3030–3033. https://doi.org/10.1039/c7cc00119c.

Xiao, X., Liu, C.Y., He, Q., Han, M.J., Meng, M., Lei, H., and Lu, X. (2013). Control of the charge distribution and modulation of the Class III—III transition in weakly coupled Mo_2-Mo_2 systems. Inorg. Chem. *52*, 12624–12633. https://doi.org/10.1021/ic4017855.

Yanai, T., Tew, D.P., and Handy, N.C. (2004). A new hybrid exchange–correlation functional using the Coulomb-attenuating method (CAM-B3LYP). Chem. Phys. Lett. *393*, 51–57. https://doi.org/10.1016/j.cplett.2004.06.011.

Zhu, G.Y., Qin, Y., Meng, M., Mallick, S., Gao, H., Chen, X.L., Cheng, T., Tan, Y.N., Xiao, X., Han, M.J., et al. (2021). Crossover between the adiabatic and nonadiabatic electron transfer limits in the Landau-Zener model. Nat. Commun. *12*, 456. https://doi.org/10.1038/s41467-020-20557-7.

STAR★METHODS

KEY RESOURCES TABLE

REAGENT or RESOURCE	SOURCE	IDENTIFIER
Chemicals, Peptides, and Recombinant Proteins		
Molybdenum hexacarbonyl (98%)	Sigma Aldrich	CAS# 13,939-06-5
p-Anisidine (99%)	Aladdin	CAS# 104-94-9
Tetrahydrofuran (Anhydrous, 99.9%)	Aladdin	CAS# 109-99-9
Oxalic acid (AR, 98%)	Aladdin	CAS# 144-62-7
Ethanol (Anhydrous grade, 99.5%)	Aladdin	CAS# 64-17-5
Ferrocenium hexafluorophosphate (97%)	Sigma Aldrich	CAS# 11077-24-0

RESOURCE AVAILABILITY

Lead contact

Further information and requests for resources and reagents should be directed to and will be fulfilled by the lead contact, Chun Y. Liu (tcyliu@jnu.edu.cn).

Materials availability

This work is a combined experimental and theoretical study on intramolecular electron transfer in mixed-valence systems and there is no new code generated.

Data and code availability

The X-ray crystallographic data of $1 \cdot 3CH_2Cl_2$ and $3 \cdot 6CH_2Cl_2$ from DCM, $1 \cdot 3C_6H_6$, $2 \cdot 5.5C_6H_6$ and $3 \cdot 4C_6H_6$ from benzene and $1 \cdot 2C_6H_6$, $2 \cdot 3C_6H_6 \cdot 2C_6F_6$ and $3 \cdot 4C_6H_6$ from hexafluorobenzene reported in this study have been deposited at the Cambridge Crystallographic Data Centre (CCDC), under deposition number CCDC 2075227, 2072627, 2072623, 2072625, 2072624, 2072622, 2072626 and 2072628.

These data can be obtained free of charge from The Cambridge Crystallographic Data Centre via www.ccdc.cam.ac.uk/data_request/cif.

The data that support the findings of this study are available from the lead contact upon reasonable request.

EXPERIMENTAL MODEL AND SUBJECT DETAILS

All manipulations were performed in a nitrogen-filled glove box or by using standard Schlenk-line techniques. All solvents were purified using a vacuum atmosphere solvent purification system or freshly distilled over appropriate drying agents under nitrogen. Starting materials HDIppF (Lin et al., 1996) and $Mo_2(DIppF)_3(O_2CCH_3)$ (Cotton et al., 2003), and dipotassium 1,2-dithiooxlate (K$_2$dto) (Tan et al., 2017) and potassium tetrathiooxalate (K$_2$tto) (Tkachov et al., 2017) were synthesized according to published methods. Complexes were variously characterized by cyclic voltammetry, single-crystal XRD, NMR, MS, EA, EPR, and UV–vis–NIR spectroscopy. The mixed-valence complexes were prepared by one-electron oxidation of the corresponding neutral compounds using one equivalent of ferrocenium hexafluorophosphate, of which the spectra were recorded *in situ*.

METHOD DETAILS

Synthesis of complex 1

A solution of $Mo_2(DIppF)_3(O_2CCH_3)$ (0.250 g, 0.229 mmol) in 10 mL of dichloromethane was transferred to a 50 mL Schlenk flask, and then a solution of oxalic acid (0.12 mmol, 0.011 g) in 10 mL of ethanol was slowly added. After stirring 10 min the solution was evaporated under reduced pressure, producing a red solid. The product was washed with ethanol (3 × 20 mL) and collected by filtration. Yield of **1**: 0.275 g, 56%. ^{1}H NMR δ (ppm in CDCl$_3$): 8.60 (s, 2H, −NCHN−), 8.52 (s, 4H, −NCHN−), 6.86 (d, 16H, aromatic C−H), 6.72 (d, 8H, aromatic C−H), 6.52 (d, 16H, aromatic C−H), 6.13 (d, 8H, aromatic C−H), 2.77 (m, 12H, isopropyl

C−H), 1.16 (m, 72H, isopropyl −CH$_3$). Mass Spectrometry (MALDI-TOF) with m/z peak for Mo$_4$C$_{116}$H$_{138}$N$_{12}$O$_4$: calcd: 2148.3000, found: 2148.7234. Elemental Anal for Mo$_4$C$_{116}$H$_{138}$N$_{12}$O$_4$: calcd: C, 64.85; H, 6.48; N, 7.82. found: C, 65.67; H, 6.38; N, 7.97.

General synthesis of complexes 2 and 3

A solution of sodium methoxide in methanol (0.5 M, 1.5 mL) was transferred to a solution of Mo$_2$(DIppF)$_3$(O$_2$CCH$_3$) (0.250 g, 0.229 mmol) in 20 mL of THF. The solution was stirred for 30 min. Then, a solution of either dipotassium 1,2-dithiooxalate (0.024 g, 0.12 mmol) for **2** or potassium tetrathiooxalate (0.027 g, 0.12 mmol) for **3** in methanol (5 mL) was slowly added and the respective solutions were stirred at room temperature for 6 h. During reaction the color of the solution slowly changes to dark blue (for **2**) or light green (for **3**). The solvents were then evaporated under reduced pressure. The solid residue was dissolved in CH$_2$Cl$_2$ (15 mL) and the solution was filtered through a Celite-packed funnel. The volume of the filtrate was reduced under a vacuum to ca. 5 mL. Then 30 mL of ethanol was added, producing a solid precipitate which was washed with ethanol (3 × 20 mL) and hexane (5 mL). The solid was collected by filtration and dried under a vacuum. Yield of **2**: 0.270 g, 54%. ^{1}H NMR δ (ppm in CDCl$_3$): 8.60 (s, 2H, −NCHN−), 8.41 (s, 4H, −NCHN−), 6.88 (d, 8H, aromatic C−H), 6.81 (d, 8H, aromatic C−H), 6.67 (m, 16H, aromatic C−H), 6.44 (d, 8H, aromatic C−H), 6.07 (m, 8H, aromatic C−H), 2.70 (m, 12H, isopropyl C−H), 1.12 (m, 72H, isopropyl −CH$_3$). Mass Spectrometry (MALDI-TOF) with m/z peak for Mo$_4$C$_{116}$H$_{138}$N$_{12}$O$_2$S$_2$: calcd: 2180.4220, found: 2180.6760. Elemental Anal for Mo$_4$C$_{116}$H$_{138}$N$_{12}$O$_2$S$_2$: calcd: C, 63.90; H, 6.38; N, 7.71. found: C, 64.29; H, 6.52; N, 7.90. Yield of **3**: 0.285 g, 56%. ^{1}H NMR δ (ppm in CDCl$_3$): 8.52 (s, 4H, −NCHN−), 8.49 (s, 2H, −NCHN−), 6.87 (d, 16H, aromatic C−H), 6.64 (d, 8H, aromatic C−H), 6.52 (d, 16H, aromatic C−H), 5.94 (d, 8H, aromatic C−H), 2.72 (m, 12H, isopropyl C−H), 1.11 (m, 72H, isopropyl −CH$_3$). Mass Spectrometry (MALDI-TOF) with m/z peak for Mo$_4$C$_{116}$H$_{138}$N$_{12}$S$_4$: calcd: 2212.5440, found: 2212.635. Elemental Anal for Mo$_4$C$_{116}$H$_{138}$N$_{12}$S$_4$: calcd: C, 62.97; H, 6.29; N, 7.60. found: C, 63.27; H, 6.48; N, 7.83.

Electrochemistry

Electrochemical measurements on the neutral compounds were carried out in 0.1M tetrahexylammonium hexafluorophosphate/benzene and dichloromethane solutions. The CVs and differential pulse voltammograms were obtained using a CH Instruments model CHI660D electrochemical analyzer with Pt working and auxiliary electrodes, and Ag/AgCl reference electrode with a scan rate of 100 mV/s. Under these conditions, the redox potential for ferrocene, $E_{1/2}$(Fc$^{+/0}$), is 0.49 V. All potentials are referenced to the Ag/AgCl electrode.

X-Ray structural determination

Single-crystals of the complexes are obtained by solvent diffusion techniques. The X-ray diffraction data was collected on a Rigaku XtaLAB Pro diffractometer with Cu-Kα radiation (λ = 1.54178 Å) (CrysAlis RED, version 1.171.31.7, 2006). The empirical absorption corrections were applied using spherical harmonics, implemented in the SCALE3 ABSPACK scaling algorithm. The structures were solved using direct methods, which yielded the positions of all non-hydrogen atoms. Hydrogen atoms were placed in calculated positions in the final structure refinement. Structure determination and refinement were carried out using the SHELXS-2014 and SHELXL-2014 programs, respectively (Sheldrick, 2000).

EPR spectroscopy

The mixed-valence radicals **1$^+$**, **2$^+$**, and **3$^+$** were prepared by one-electron oxidation of the corresponding neutral compounds using one equiv of ferrocenium hexafluorophosphate (Cp$_2$FePF$_6$) in DCM and benzene solutions. The EPR measurements were carried out in $situ$ after oxidation at 100 K using a Bruker A300−10−12 electron paramagnetic resonance spectrometer and each complex shows one main signal with some hyperfine structures.

Spectroscopic measurements

For all three complexes, including the neutral and the corresponding singly oxidized MV species, the electronic spectra were measured in the UV-Visible region and vibronic intervalence charge transfer (IVCT) absorption in the near-IR region in dichloromethane, benzene, and hexafluorobenzene (5 × 10^{-4} mol dm^{-3}) using IR quartz cells with a light path length of 2 mm on a Shimadzu UV-3600 UV-vis-NIR spectrophotometer.

DFT calculations

The ORCA 4.2 software packages, which are applicable for *ab initio*, DFT, and semiemperical SCF-MO computations, were used for the theoretical work performed in this study (Neese, 2012). The geometry of the model complexes was optimized in the gas phase, employing the Becke−Perdew (BP86) functional (Perdew, 1986; Becke, 1988) and RI/J approximation (Neese, 2003). Geometry optimizations for the complexes were converged with the def2-SV(P) basis set (Schafer et al., 1992) for C and H atoms, def2-TZVP(-f) basis set (Weigend and Ahlrichs, 2005) for S, N, and O atoms, and def2-TZVPP basis set for Mo atoms including the ZORA approximation (Pantazis et al., 2008). For the calculations, the corresponding auxiliary basis set def2-SVP/J (Eichkorn et al., 1995, 1997) for C and H atoms, def2-TZVP/J (Neese, 2012) for S, N, and O atoms, and def2-TZVPP/J for Mo atoms are also used. Cartesian coordinates (Å) for DFT energy-minimized models are given in Tables S10–S22. Single-point calculations on the optimized geometries of simplified complex models **1′**, **2′**, and **3′** and supramolecular models [**1′**⊂C_6H_6-C], [**2′**⊂C_6H_6-C], [**3′**⊂C_6H_6-C], and [**3′**⊂C_6H_6-T] were performed with the range-separated CAM-B3LYP functional (Yanai et al., 2004) and TZVP basis set (Schafer et al., 1992). The *ab initio* calculations were performed to estimate the intermolecular interaction energies (E_{int}) for the simplified supramolecular structures [**1′**⊂C_6H_6-C], [**2′**⊂C_6H_6-C], and [**3′**⊂C_6H_6-C], and [**3′**⊂C_6H_6-T]. For these calculations, the coupled cluster (CC) method CCSD(T) (Rezac and Hobza, 2013; Jurecka et al., 2006; Simova et al., 2013) and aug-cc-pVDZ basis set (for C, H, N, O and S atoms) and def2-TZVPP basis set (for Mo atoms) were used.

QUANTIFICATION AND STATISTICAL ANALYSIS

The UV-vis-near IR raw data were collected on a Shimadzu UV-3600 spectrophotometer and spectral figures were drawn using Origin 8.5.

ADDITIONAL RESOURCES

Any additional information about the spectral analysis, DFT computations, and data reported in this paper is available from the lead contact on reasonable request.